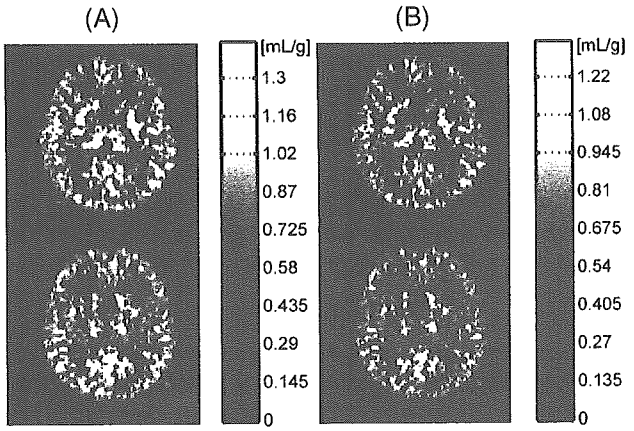

Fig. 2. Example of the parametric images of DVt calculated using the EPICA-estimated pTAC (A) and the measured arterial blood samples (B).

subject. Close agreement was obtained between the two images in all 25 subjects. Comparison between the calculated images of DVt was shown in Fig. 3. The regression line was $y = 1.07x + 0.06$ and the correlation coefficient r was 0.99. Good agreement was obtained between two images. Typical Logan plots are shown for the cerebellum, frontal, and thalamus in Fig. 4. There is good coincidence between the slopes of the plots using the measured and the EPICA-estimated pTACs.

Fig. 5 shows the TACs averaged over the refined cerebellar reference region and the excluded cerebellar region with high DVt values. The shape of two TACs is different from each other. The estimated DVt of a mean TAC in the refined reference region was 0.68 ± 0.02 and that in the excluded region was 0.82 ± 0.02. Fig. 6 shows examples of the BP images calculated using Logan plots with the EPICA-estimated pTAC. The BP images from a normal volunteer and a patient with a brain tumor are shown in Figs. 6A and B, respectively. The patient has a metastatic right tempor-ooccipital brain tumor that causes left upper quadranopsia. The BPs in the medial occipital lobe (primary visual cortex) showed low values, as shown in Fig. 6B.

Correlations of BP values calculated using NLSM and the present method are shown in Fig. 7 for 18 subjects: 11 healthy volunteers and 7 patients (temporal lobe epilepsy, 3; Alzheimer disease, 1; Parkinson disease, dementia, or dementia with Lewy bodies, 1; cerebrovascular disease, 1; and brain tumor, 1). The total

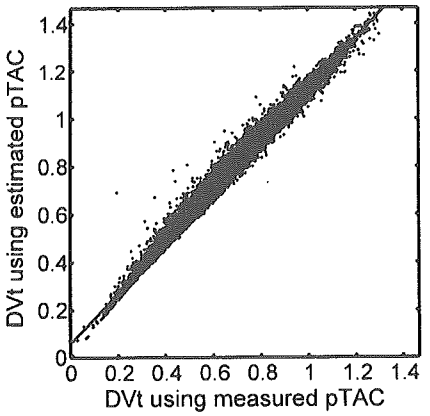

Fig. 3. Scatter plot between the parametric images of DVt estimated using the EPICA-estimated pTAC and the measured pTAC. A total of 60,241 voxels were plotted.

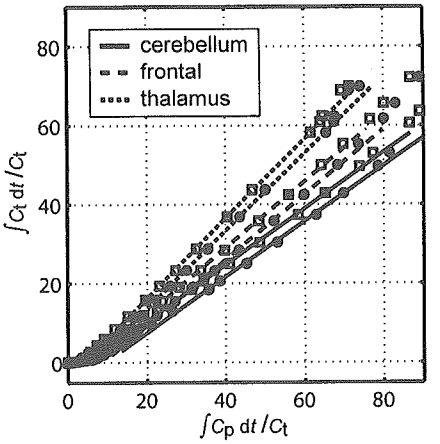

Fig. 4. Typical Logan plots for the cerebellum, frontal, and thalamus. The plots using the EPICA-estimated pTAC and the measured pTAC are represented by squares and circles, respectively. The regression lines were derived from 10 to 40 min after the administration.

of 126 ROIs were used for the evaluation. The regression line was $y = 0.96x + 0.03$ and the correlation coefficient r was 0.90. There was close agreement between both calculated results.

Discussion

The EPICA technique was developed as a method for extracting an input function from the PET images to eliminate arterial blood sampling in kinetic analysis of [^{18}F]FDG PET (Naganawa et al., 2003, 2005). In the present study, we investigated the suitability of the EPICA procedure in neuroreceptor mapping. EPICA does not assume kinetics of tracers, and the EPICA technique is expected to be able to extract the pTAC from the [^{11}C]MPDX PET images without any modification. Fig. 1 shows that the estimated pTAC was in close agreement with the measured pTAC. EPICA successfully extracted the pTAC in all subjects in [^{11}C]MPDX PET, as was previously demonstrated for [^{18}F]FDG PET. While the peak of the estimated pTAC deviated slightly from the measured pTAC immediately after [^{11}C]MPDX administration, both pTACs matched closely at 3 min or later after administration. The deviation was found in all subjects. The scan interval in an initial

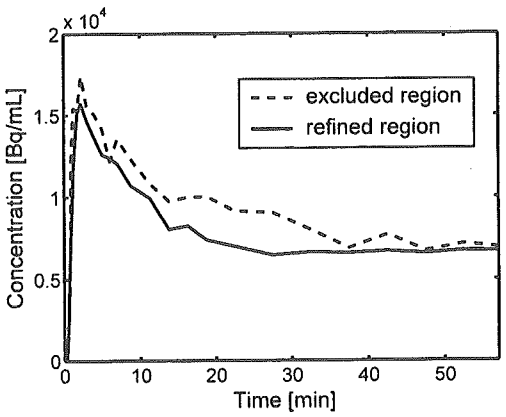

Fig. 5. Example of a TAC averaged over the cerebellar region with DVt values than the 80th percentile (break line) and a TAC averaged over the refined cerebellar region with threshold (solid line).

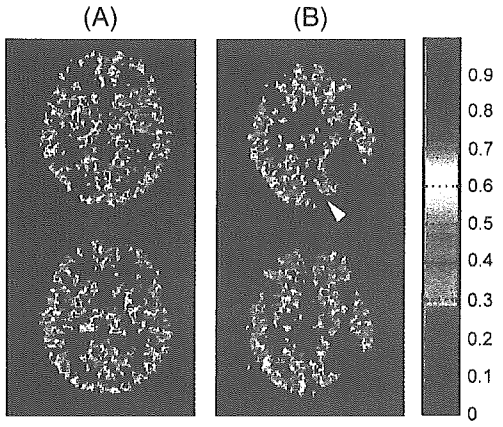

Fig. 6. Examples of the calculated parametric image of BP in a normal brain (A) and brain with a tumor (B). Arrows denote the affected region. The values of BP in the medial occipital lobe (primary visual cortex) are low. These images were calculated from the DVt images estimated using the EPICA-estimated pTAC and a reference region.

3 min should be short enough to capture the rapid change of pTAC. Therefore, signal to noise ratio of the data is relatively low in the first 3 min, which causes the variation in the pTAC estimation. The slight deviation scarcely affects the accuracy of the estimation of DVt because Logan plots were applied to the dynamic PET images after 10 min (Kimura et al., 2004).

The EPICA-estimated pTAC has indeterminacy in its amplitude because of the mathematical limitations of ICA. However, the determination of the amplitude of the EPICA-estimated pTAC was not required when calculating BP. According to Eq. (7), BP can be calculated from the relative value of DVt. Therefore, no arterial blood sampling is needed. One-point arterial blood sampling would be required if an absolute value was needed; for instance, in cases of calculating the absolute value of DVt. It is also beneficial for neuroreceptor imaging that EPICA gives us the relative values of DVt and the reference region can be refined based on the DVt values. The spatial distributions of the parametric image using the EPICA-estimated and measured pTACs were similar, as shown in Figs. 2 and 3. The slopes of Logan plots using the estimated and the measured pTACs were coincident as shown in Fig. 4. The difference in their intercepts is due to the difference in the initial part of the pTACs.

There are two theoretical considerations about the EPICA-estimated pTAC: plasma and whole blood TACs, and metabolic correction. Because estimation of TACs is based on spatial distributions of the blood vessels and brain tissue, EPICA estimates TACs that correspond to a whole blood and brain tissue. Both whole blood and plasma TACs originated from blood, and they have same spatial distributions. Consequently, EPICA cannot distinguish their difference. Moreover, EPICA does not distinguish a metabolite form from an administered tracer. However, in case of [^{11}C]MPDX, its metabolite form is negligible (Kimura et al., 2004). According to the previous investigation, 76% of the administered [^{11}C]MPDX retained its intact form at 60 min after administration. The plasma/whole blood ratio kept constant in the duration where Logan plot was applied. The pTAC with a metabolite correction is approximately equal to a whole blood TAC without a metabolite correction in estimating relative DVts by Logan plot. Note that the effect of metabolite to the estimates and the plasma/whole blood ratio should be investigated before applying the proposed framework to other tracer's dynamic PET data.

There are several methods of estimating BP or DV ratio, which is equal to BP − 1, without arterial blood sampling. The method proposed by Logan et al. (1996) requires the average value of k_2 in the ROI to be estimated in advance, but it is difficult to assume the value of k_2, and it is impossible in cases of generating parametric images of BP because k_2 should be assumed for each voxel. In the present method, no assumptions about kinetic parameters are required. Gunn et al. (1997) proposed a method of estimating BP using a simplified reference region model based on a basis function approach. This basis function method estimates the parameters BP, K_1/K_1', and k_2 simultaneously (K_1' describes the kinetic parameter in a reference region). Our method refines the manually drawn reference region using the estimated DVt values. The DVt image shows directly the regions in the brain where A1R is poor. Note that our method allows generation of parametric images of DVt and BP, whereas Gunn's method provides parametric images of K_1/K_1', k_2, and BP using a predefined reference region. As shown in Fig. 5, the TAC averaged over the region with high DVt values was different from that averaged over the refined region, which suggests that the roughly defined reference region has a specific binding. In the present study, the 80th percentile value was empirically chosen as the practical optimal threshold. The EPICA-based BP estimation was confirmed by ROI-based comparison with the BP calculated by NLSM. In each subject, there was close agreement between both parameters as shown in Fig. 7.

Omission of arterial blood sampling has a great advantage in neuroreceptor mapping. The availability of the proposed method was first demonstrated in [^{11}C]MPDX PET. Further application of the method to different neuroreceptor radioligands is now ongoing. In addition, the method will extend to pediatric studies or small animal studies, where blood quantity is limited and no blood can be wasted.

Conclusion

The present method generates parametric images of DVt and BP without arterial blood sampling by using Logan plots and EPICA. We performed validation of the estimated DVt and BP, and confirmed that the estimates were comparable to those using the

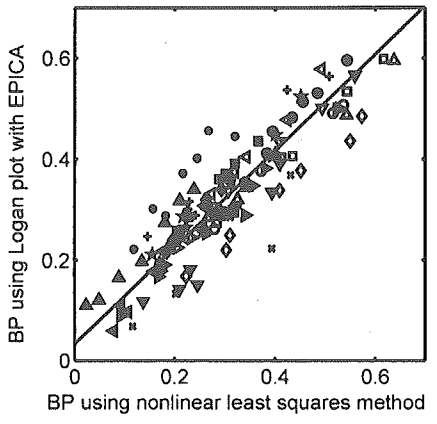

Fig. 7. Comparison of BPs calculated using NLSM or Logan plots with EPICA. Each symbol represents one subject.

measured pTAC. We concluded that EPICA is a useful technique for eliminating arterial blood sampling from neuroreceptor mapping studies.

Acknowledgment

The authors thank Dr. Fukumitsu (Department of Radiology, Jikei University School of Medicine) for providing some of the clinical PET data. This work is supported in part by the Grants-in-Aid for Scientific Research by the Japan Society for the Promotion of Science, No. 16591243 in 2004 and 2005 and No. 16390348 in 2004–2006, and the Grant-in-Aid for the 21st Century COE from the Ministry of Education, Culture, Sports, Science and Technology of Japan.

References

Bedford, R.F., Wallman, H., 1973. Complications of percutaneous radial-artery cannulation: an objective prospective study in man. Anesthesiology 38, 228–236.

Bell, A.J., Sejnowski, T.J., 1995. An information maximisation approach to blind separation and blind deconvolution. Neural Comput. 7, 1129–1159.

Comon, P., 1994. Independent component analysis, a new concept? Signal Process. 36, 287–314.

Fastbom, J., Pazos, A., Probst, A., Palacios, J., 1987. Adenosine A_1 receptors in the human brain: a quantitative autoradiographic study. NeuroImage 22, 827–839.

Fukumitsu, N., Ishii, K., Kimura, Y., Oda, K., Sasaki, T., Mori, Y., Ishiwata, K., 2003. Imaging of adenosine A_1 receptors in the human brain by positron emission tomography with [^{11}C]MPDX. Ann. Nucl. Med. 17, 511–515.

Fukumitsu, N., Ishii, K., Kimura, Y., Oda, K., Sasaki, T., Mori, Y, Ishiwata, K., 2005. Adenosine A_1 receptor mapping of the human brain by positron emission tomography with [^{11}C]MPDX. J. Nucl. Med. 46, 32–37.

Gunn, R.N., Lammertsma, A.A., Hume, S.P., Cunningham, V.J., 1997. Parametric imaging of ligand-receptor in PET using a simplified reference region model. NeuroImage 6, 279–287.

Hyvärinen, A., 1999. Fast and robust fixed-point algorithms for independent component analysis. IEEE Trans. Neural Netw. 10, 626–634.

Hyvärinen, A., Oja, E., 1997. A fast fixed-point algorithm for independent component analysis. Neural Comput. 9, 1483–1492.

Ishiwata, K., Nariai, T., Kimura, Y., Oda, K., Kawamura, K., Ishii, K., Senda, M., Wakabayashi, S., Shimada, J., 2002. Preclinical studies on [^{11}C]MPDX for mapping adenosine A_1 receptors by positron emission tomography. Ann. Nucl. Med. 16, 377–382.

Jons, P.H., Ernst, M., Hankerson, J., Hardy, K., Zametkin1, A.J., 1997. Follow-up of radial arterial catheterization for positron emission tomography studies. Hum. Brain Mapp. 5, 119–123.

Kimura, Y., Ishii, K., Fukumitsu, N., Oda, K., Sasaki, T., Kawamura, K., Ishiwata, K., 2004. Quantitative analysis of adenosine a1 receptors in human brain using positron emission tomography and [1-methyl-^{11}C]8-dicyclopropylmethyl-1-metyl-3-propylxanthine. Nucl. Med. Biol. 31, 975–981.

Logan, J., 2000. Graphical analysis of PET data applied to reversible and irreversible tracers. Nucl. Med. Biol. 27, 661–670.

Logan, J., Fowler, J.S., Volkow, N.D., Wolf, A.P., Dewey, S.L., Schlyer, D.J., MacGregor, R.R., Hitzmann, R., Bendriem, B., Gatley, S.J., Christman, D.R., 1990. Graphical analysis of reversible radioligand binding from time–activity measurements applied to [n-^{11}C-methyl]-(−)-cocaine PET studies in human subjects. J. Cereb. Blood Flow Metab. 10, 740–747.

Logan, J., Fowler, J.S., Volkow, N.D., Wang, G.-J., Ding, Y.-S., Alexo, D.L., 1996. Distribution volume ratios without blood sampling from graphical analysis of PET data. J. Cereb. Blood Flow Metab. 16, 834–840.

McKeown, M.J., Makeig, S., Brown, G.G., Jung, T.-P., Kindermann, S.S., Bell, A.J., Sejnowski, T.J., 1998. Analysis of fMRI data by blind separation into independent spatial components. Hum. Brain Mapp. 6, 160–188.

Mintun, M.A., Raichle, M.E., Kilbourn, M.R., Wooten, G.F., Welch, M.J., 1984. A quantitative model for the in vivo assessment of drug binding sites with positron emission tomography. Ann. Neurol. 15, 217–227.

Naganawa, M., Kimura, Y., Matani, A., 2003. Modification of ICA for extracting blood vessel-related component in nuclear medicine: contrast function and nonnegative constraints. Proceedings ICA2003. ICA, Nara, Japan, pp. 65–71.

Naganawa, M., Kimura, Y., Ishii, K., Oda, K., Ishiwata, K., Matani, A., 2005. Extraction of a plasma time–activity curve from dynamic brain PET images based on independent component analysis. IEEE Trans. Biomed. Eng. 51, 201–210.

Svenningsson, P., Hall, H., Sedvall, G., Fredholm, B.B., 1997. Distribution of adenosine receptors in the postmortem human brain: an extended autoradiographic study. Synapse 27, 322–335.

Aortic Wall Inflammation Due to Takayasu Arteritis Imaged with ^{18}F-FDG PET Coregistered with Enhanced CT

Yasushi Kobayashi, MD, PhD[1,2]; Kenji Ishii, MD[3]; Keiichi Oda, PhD[3]; Tadashi Nariai, MD, PhD[4]; Youji Tanaka, MD[4]; Kiichi Ishiwata, PhD[3]; and Fujio Numano, MD, PhD[1]

[1]Department of Internal Medicine, Tokyo Medical and Dental University, Tokyo, Japan; [2]Section of Immunobiology, Yale University School of Medicine, New Haven, Connecticut; [3]Positron Medical Center, Tokyo Metropolitan Institute of Gerontology, Tokyo, Japan; and [4]Department of Neurosurgery, Tokyo Medical and Dental University, Tokyo, Japan

The purpose of this study was to evaluate the ability of ^{18}F-FDG PET to identify aortitis and to localize and follow disease activity in patients with Takayasu arteritis. The value of using ^{18}F-FDG PET coregistered with enhanced CT in determining vascular lesion sites and inflammatory activity was assessed. **Methods:** Takayasu arteritis was diagnosed according to the predefined criteria. Eleven patients with Takayasu arteritis in the active stage, 3 patients with Takayasu arteritis in the inactive stage, and 6 healthy subjects underwent ^{18}F-FDG PET coregistered with enhanced CT and the inflammatory vascular lesion was evaluated by using the standardized uptake value (SUV) of ^{18}F-FDG accumulation as an index. Two patients with active disease were analyzed by sequential ^{18}F-FDG PET scans during treatment. **Results:** The ^{18}F-FDG PET revealed intense ^{18}F-FDG accumulation (SUV $\geq$ 2.7) in the vasculature of 2 of the 11 cases in the active stage of Takayasu arteritis. The other 9 patients in the active stage revealed weak ^{18}F-FDG accumulation (2.3 $\geq$ SUV $\geq$ 1.2). No significant ^{18}F-FDG accumulation was observed in the patients with inactive disease (SUV $\leq$ 1.2) and 6 control healthy subjects (SUV $<$ 1.3). Given the cutoff SUV is 1.3, the sensitivity of ^{18}F-FDG PET analysis of Takayasu arteritis is 90.9% and the specificity is 88.8%. ^{18}F-FDG PET coregistered with enhanced CT localized ^{18}F-FDG accumulation in the aortic wall in the patients with Takayasu arteritis who had weak ^{18}F-FDG accumulation that could not otherwise be identified anatomically. Finally, ^{18}F-FDG accumulation resolved with therapy in 2 active cases. The disappearance of ^{18}F-FDG accumulation did not coincide with the level of general inflammatory markers. **Conclusion:** The ^{18}F-FDG PET images coregistered with enhanced CT images showed the distribution and inflammatory activity in the aorta, its branches, and the pulmonary artery in patients with active Takayasu arteritis, even those who had weak ^{18}F-FDG accumulation. The intensity of accumulation decreased in response to therapy.

Key Words: aortitis; Takayasu arteritis; PET; ^{18}F-FDG; CT

J Nucl Med 2005; 46:917–922

Received Oct. 22, 2004; revision accepted Jan. 27, 2005.

For correspondence or reprints contact: Kenji Ishii, MD, Positron Medical Center, Tokyo Metropolitan Institute of Gerontology, 35-2 Sakaecho, Itabashi, Tokyo 173-0015 Japan.

E-mail: ishii@pet.tmig.or.jp

Takayasu arteritis is an idiopathic systemic granulomatous disease of large- and medium-sized vessels that may lead to vascular lesions such as segmental stenosis, occlusion, dilatation, and aneurysm formation in the aorta and its main branches (*1,2*). It mainly affects young females. Its pathogenesis is still unknown.

The diagnosis of Takayasu arteritis is made from the identification of a vascular lesion by a conventional aortogram, enhanced CT, MRI, augmented general inflammatory markers, or clinical symptoms due to ischemia. The disease activity of Takayasu arteritis is estimated from the levels of general inflammatory markers such as C-reactive protein and erythrocyte sedimentation rate during treatment with medication. However, general inflammatory markers usually are not good surrogate markers for evaluating the disease activity of Takayasu arteritis (*3*).

Gadolinium-enhanced MRI has been recently reported to provide imaging adequate to delineate large vessel anatomy and identify stenotic lesions (*4*). In gadolinium-enhanced MRI, the enhanced uptake of contrast agent by the inflamed large vessels are presumably due to enhanced permeability. However, the specificity for active inflammation or edema in the vessel wall is imperfect. Histopathology remains the gold standard for active vascular inflammation and it cannot be done in the diagnosis of Takayasu arteritis (*5*).

^{18}F-FDG PET has been recently reported to be useful in the diagnosis of vascular diseases such as atherosclerosis and large vessel aortitis (*6–12*). However, we found that most of the patients with active Takayasu arteritis revealed weak ^{18}F-FDG accumulation in the vascular wall of the large vessels by PET analysis and therefore we could not diagnose Takayasu arteritis by ^{18}F-FDG PET alone. And few cases were studied to determine whether ^{18}F-FDG accumulation might disappear in response to the medication.

The aim of our study was to evaluate whether ^{18}F-FDG PET coregistered with enhanced CT can identify the distribution of the inflammation in the vasculature, facilitate the diagnosis anatomically, and evaluate the disease activity of

Takayasu arteritis. We also evaluated whether there are differences between the disease activity estimated by general inflammatory markers and that estimated by ^{18}F-FDG PET. We prospectively studied 11 patients with active Takayasu arteritis, 3 patients with inactive Takayasu arteritis, according to the diagnostic criteria (*13*) and 6 healthy control subjects. The coregistration of PET with enhanced CT may facilitate the diagnosis of Takayasu arteritis and could validate the usefulness of ^{18}F-FDG PET for evaluating the disease activity of Takayasu arteritis

MATERIALS AND METHODS

Selection of Patients and Control Subjects

The study included 14 patients (13 women, 1 man) with Takayasu arteritis according to the American College of Rheumatology criteria (*13*). Of the 14 patients, 11 were in the acute stage and 3 were in the chronic stage. The mean age was 28 y old (range, 14–50 y old). Details of the patients are summarized in Table 1. All patients in acute stage were given 30 mg of prednisolone. In some cases with strong inflammation, 100 mg of cyclosporine were given together with prednisolone. The acute stage patient is defined as the patient with Takayasu arteritis who needs prednisolone to control the inflammation in the vessel clinically. And the chronic stage patient is defined as the patient with Takayasu arteritis who no longer need prednisolone for at least 2 y. Six control subjects without Takayasu arteritis were also studied. All participants were Japanese. Written informed consent was obtained from all participants before the study began. This study was approved by the Institutional Ethical Committee.

CT Scan

Standard diagnostic CT scans were performed on a spiral CT scanner with 5-mm center-to-center slice separation, 512 × 512 matrix size, 0.54- to 0.82-mm pixel size, and 39–85 axial slices that include the neck and the entire lung volume. Scans were performed with intravenous contrast. During the scan, patients raised their arms and held their breath.

^{18}F-FDG PET

PET was performed with a whole-body PET scanner, model SET 2400W (Shimadzu Co.), with an axial field of view of 20.0 cm and 63 transverse slices with a slice thickness of 3.125 mm. ^{18}F-FDG was produced using a commercial kit (FDG MicroLab; GE Healthcare) in the Positron Medical Center, Tokyo Metropolitan Institute of Gerontology. All patients were asked to fast for >12 h before the study to minimize glucose utilization in normal tissues and to ensure standardized glucose metabolism. A total of 23 rounds of ^{18}F-FDG PET scans were performed in 14 patients with Takayasu arteritis; each of 6 healthy subjects underwent ^{18}F-FDG PET once. The image acquisition on 2-dimensional mode started 45 min after the intravenous administration of 300–370 MBq (approximately 6 MBq ^{18}F-FDG per kilogram of body weight) using simultaneous emission and transmission measurement methods (*14*). A 7-min emission/transmission scan with a ^{68}Ga/^{68}Ge rotating rod source was performed for 4 overlapping bed positions; this resulted in an axial field of view of 75 cm and a total acquisition time of 28 min. Emission and transmission sinograms were separated by the sinogram windowing technique. The transmission scan for the attenuation correction was filtered using nonlinear gaussian filters to reduce noise (*15*) and reconstructed using ordered-subsets expectation maximization with 6 iterations and 16 subsets and postsmoothed using a 3 × 3 × 3 cubic filter. The image pixel counts were calibrated to activity concentration (Bq/mL) and were corrected for decay using the time of tracer injection as the reference. The resulting in-plane image resolution of the transaxial image was approximately 8-mm full width at half maximum.

TABLE 1
Details of Patients with Takayasu Arteritis Who Underwent ^{18}F-FDG PET

Patient no.	Sex	Age (y)	Disease stage	CRP (mg/L)	ESR (mm/h)	FBS (mg/dL)	Maximal SUV*	^{18}F-FDG site
1	F	17	Active	80	95	110	1.8	As, SC
2	F	27	Active	72	97	91	1.7	Ar, CC
3	F	21	Active	14	88	107	3.5	Ve
4	F	37	Active	21	78	96	2.7	As
5	F	31	Active	11	33	80	2.0	As, Ds
6	M	21	Active	65	24	97	2.3	As
7	F	33	Active	41	94	88	1.8	As
8	F	25	Active	50	85	96	1.9	As
9	F	14	Active	25	45	82	1.2	As
10	F	24	Active	16	85	93	1.9	As, Ds
11	F	21	Active	17	54	138	1.4	CC
12	F	50	Inactive	0	15	99	1.2	As
13	F	39	Inactive	3	49	90	1.2	As
14	F	44	Inactive	0	12	88	1.2	As
Control subjects†	1 M, 5 F	22–74		Negative	Negative	66–95	1.1 ± 0.2‡	As

*Maximal SUVs were evaluated at highest ^{18}F-FDG accumulation sites on first PET scan.
†n = 6.
‡Mean ± SD.
CRP = C-reactive protein; ESR = erythrocyte sedimentation rate; FBS = fasting blood sugar; As = ascending aorta; SC = subclavian arteries; Ar = aortic arch; CC = common carotid arteries; Ve = vertebral arteries; Ds = descending artery.

Initial Data Processing

Further data processing and analysis were performed on an SGI workstation (Silicon Graphics) using Dr.View software (Asahi Kasei Joho System). Before image registration, the PET data were resampled to a 256 × 256 matrix and the volume extents and pixel sizes were adjusted automatically by our registration software to equalize the extents of PET and CT field of view. The coregistration of PET and enhanced CT was obtained by the semiautomated process of rigid-body transformation with additional fine adjustment of the interactive process of viewing the superimposed images in 3-dimensional slices using the Dr.View program so that the outline of the mediastinum and the upper edge of the lung were matched. With this approach, satisfactory registration was achieved at the particular region of the thoracic aorta and its branching portions regardless of the arm position.

Visual Analysis

PET data were analyzed by visual interpretation of coronal, sagittal, and transverse slices and cross-referenced with coregistered enhanced CT images and rotating 3-dimensional images when necessary. All 3 image modalities (CT, PET, and coregistered images) were assessed separately by 2 experienced radiologists using standardized questionnaires independently. The aorta was considered positive for aortitis when heterogeneously increased ^{18}F-FDG uptake was present in areas presumed to correspond to the aorta in the enhanced CT images. In contrast, the aorta was considered negative when no ^{18}F-FDG uptake was observed.

Analysis of Regions of Interest (ROIs)

Each ROI was identified on the wall of the aorta with its center on the local maximum of ^{18}F-FDG accumulation by the same nuclear medicine physician during the entire study. ^{18}F-FDG uptake was quantified at the ROI using the standardized uptake value (SUV) normalized for lean body mass. In the control case, ^{18}F-FDG uptake was quantified at the aortic arch because Takayasu arteritis affects the aortic arch most often. The SUV is defined as a tissue activity concentration divided by the total activity injected per body weight.

RESULTS

^{18}F-FDG Accumulation in Vascular Walls of Patients with Active Takayasu Arteritis

As shown in Table 1, in 2 patients with active disease, strong ^{18}F-FDG accumulation (SUV ≥ 2.7), which was easily identified in the aortic region, was observed and the other patients with active disease revealed weak ^{18}F-FDG accumulation (2.3 ≥ SUV ≥ 1.2), from which identification of the location of ^{18}F-FDG accumulation was difficult by ^{18}F-FDG PET alone. Furthermore, ^{18}F-FDG accumulation in this study did not always coincide with established aortic lesions observed in CT or MR angiography. In contrast, 3 patients with inactive disease (SUV = 1.2) and the control subjects had no specific ^{18}F-FDG accumulation in the vasculature and revealed low SUVs (SUV < 1.3) in the aortic arch region. Therefore, we judged that the cutoff point of SUV could be 1.3 for the diagnosis of vascular inflammation in our analysis. Given the SUV cutoff point is 1.3, the sensitivity of our analyses should be 90.9% and the specificity should be 88.8%.

^{18}F-FDG PET Coregistered with Enhanced CT Facilitates Identification of ^{18}F-FDG Accumulation of Takayasu Arteritis Anatomically

As shown in Table 1, most of the patients with active disease did not have strong ^{18}F-FDG accumulation that was easily identified in the aortic region. Therefore, to identify the lesion of ^{18}F-FDG accumulation anatomically, we coregistered the ^{18}F-FDG PET images with the enhanced CT images.

In the case shown in Figure 1, enhanced CT showed a dilated aortic arch causing severe aortic regurgitation and constriction of the abdominal aorta due to Takayasu arteritis. Similar findings were confirmed in the angiogram and MR images (data not shown). The ^{18}F-FDG accumulation was observed in the mediastinum region (Figs. 1A and 1D), but we could not adequately identify whether these ^{18}F-FDG accumulations were located in the vascular wall on the basis of the PET image alone. However, as shown in Figures 1B and 1E, the ^{18}F-FDG PET images coregistered with enhanced CT images revealed that these ^{18}F-FDG accumulations were localized in the vascular wall of the ascending arteries and also in the pulmonary arteries. These ^{18}F-FDG accumulations did not always coincide with a vascular wall thickening lesion. These may represent areas of inflammation that have not yet progressed to develop vascular thickening.

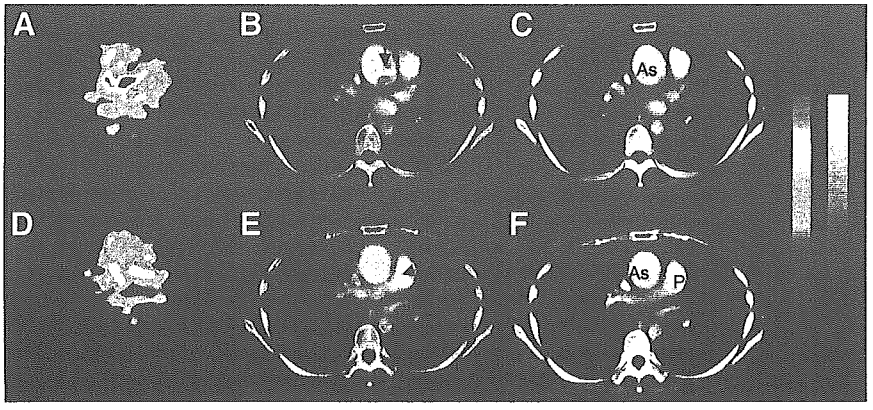

FIGURE 1. A 37-y-old woman with active Takayasu arteritis. ^{18}F-FDG PET coregistered with enhanced CT revealed that ^{18}F-FDG accumulations were localized in vascular wall of ascending aortic and pulmonary artery. (A and D) Axial images of ^{18}F-FDG PET. ^{18}F-FDG accumulated in mediastinum. (B and E) Coregistered PET with enhanced CT images. Arrows indicate ^{18}F-FDG accumulation in ascending aorta (B) and pulmonary arteries (E). (C and F) Enhanced reconstituted CT images of same level of A and D. Ascending aorta was enlarged, causing aortic regurgitation. As = ascending aorta; P = pulmonary artery.

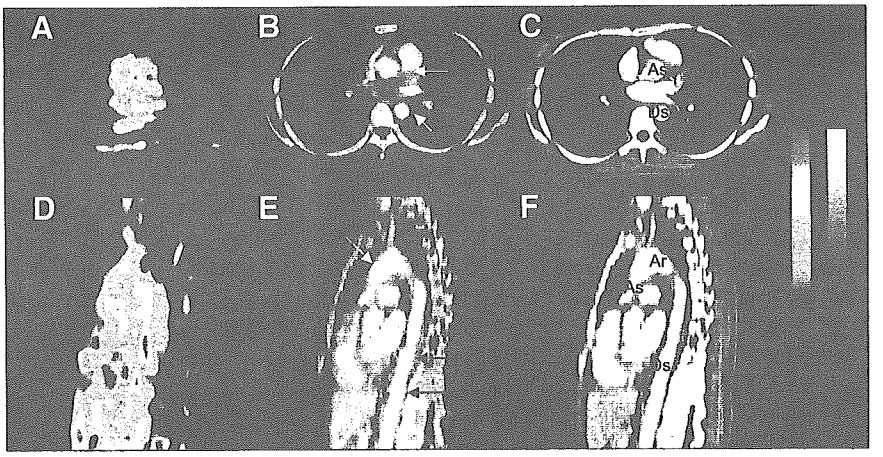

FIGURE 2. A 31-y-old woman with active Takayasu arteritis. ^{18}F-FDG PET coregistered with enhanced CT revealed that ^{18}F-FDG accumulations were localized in vascular wall of ascending aorta, aortic arch, and descending artery. (A and D) Axial (A) and sagittal (D) images of ^{18}F-FDG. (B and E) Coregistered PET with enhanced CT images. ^{18}F-FDG accumulation was observed in mediastinum and region along spine. Arrows show ^{18}F-FDG accumulations in aorta. (C and F) Enhanced reconstituted CT images of same section of A and C. As = ascending aorta; Ds = descending aorta; Ar = aortic arch.

^{18}F-FDG PET Coregistered with Enhanced CT Facilitates Diagnosis of the Suspected Case of Takayasu Arteritis

In the case shown in Figure 2, we observed the wall thickness of both common carotid arteries by carotid echography but did not locate a clear vascular deformity by the angiogram, MRI, and enhanced CT (Figs. 2C and 2F). In this case, weak ^{18}F-FDG accumulation was observed in ^{18}F-FDG PET (Figs. 2A and 2C) and we could not diagnose Takayasu arteritis by ^{18}F-FDG PET alone. However, ^{18}F-FDG PET coregistered with enhanced CT showed that the ^{18}F-FDG accumulations were located in the ascending aortic wall (Fig. 2B), in the aortic arch, and in the descending aorta (Figs. 2B and 2E). Interestingly, in the carotid artery, where wall thickness was observed, ^{18}F-FDG accumulation was not evident. In this case, although marked deformity of a large vessel was not observed, ^{18}F-FDG accumulation was identified in the aortic walls by these coregistered images, facilitating the diagnosis of suspected Takayasu arteritis.

^{18}F-FDG Accumulation in Vasculature Disappeared During Treatment with Medication and Did Not Correlate with General Inflammatory Markers

We performed 4 sequential ^{18}F-FDG PET analyses of a patient with active Takayasu arteritis to determine whether these ^{18}F-FDG accumulations disappear during medical therapy (Fig. 3). The patient was given 30 mg of prednisolone daily. The inflammatory markers were normalized in a week. In contrast, the ^{18}F-FDG accumulation apparent in ^{18}F-FDG PET was not diminished for many months and did not correlate with the normalization of general inflammatory markers (Fig. 3). ^{18}F-FDG accumulation was almost diminished within 6 mo after the combination therapy of 30 mg of prednisolone and 100 mg of cyclosporine (Fig. 3). The other patient who underwent sequential PET analysis also showed diminished ^{18}F-FDG accumulation with 30 mg of prednisolone and 100 mg of cyclosporine (data not shown). We also examined the reproducibility using a sequential PET analysis shown in Figure 3 at her nonaffected descending aorta. The SUVs in each PET analysis were

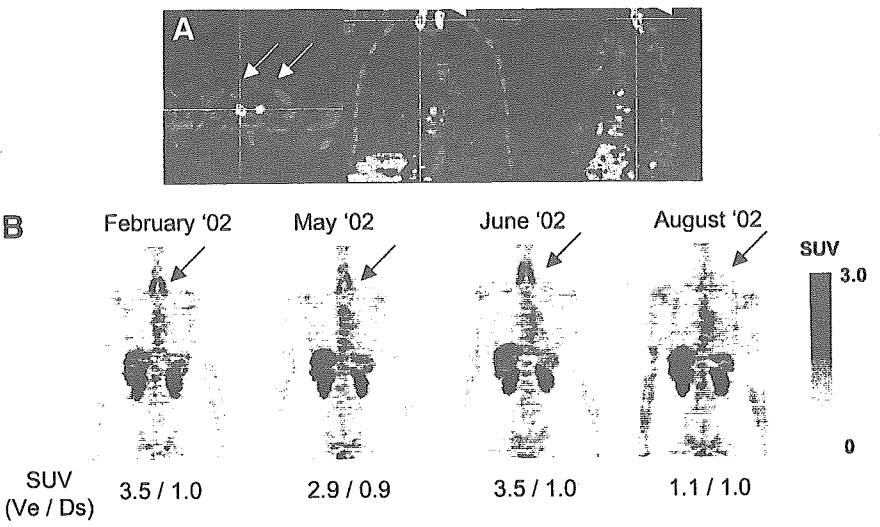

FIGURE 3. A 21-y-old woman with active Takayasu arteritis. (A) Increased ^{18}F-FDG was identified at both vertebral arteries by ^{18}F-FDG PET coregistered with CT (white arrows). (B) Four sequential ^{18}F-FDG PET analyses showed that ^{18}F-FDG accumulations in vertebral arteries on both sides disappeared during treatment with prednisolone and cyclosporine (black arrows). SUVs at bottom of each image were measured at peak signals in left side of vertebral artery (Ve) with active inflammation and at descending aorta (Ds) without inflammatory activity as a reference.

1.05, 0.91, 0.96, 1.03, and 1.19. Therefore, we believe the ^{18}F-FDG PET data are reproducible and these data can be compared together.

DISCUSSION

This study is a prospective analysis of the utility of ^{18}F-FDG PET coregistered with enhanced CT in the localization of inflammation in the large vessels and estimation of the inflammatory activity in patients with Takayasu arteritis. In this study, we found that ^{18}F-FDG PET analysis of Takayasu arteritis alone did not always give a signal strong enough to demonstrate inflammation of a vascular lesion; ^{18}F-FDG PET coregistered with enhanced CT can enhance the sensitivity of the ^{18}F-FDG accumulation in the aorta, its branches, and the pulmonary artery due to Takayasu arteritis and also can estimate the disease activity. We also showed that the ^{18}F-FDG accumulation responded to medication and disappeared. The disappearance did not coincide with the level of the general inflammatory markers. In contrast, in the patients with inactive Takayasu arteritis and the healthy subjects, low ^{18}F-FDG accumulation was observed in the vascular wall. These findings suggest that the ^{18}F-FDG accumulation observed in the patients with active Takayasu arteritis indicates the site of inflammation in the affected vascular lesion.

The diagnosis of Takayasu arteritis is made from image analysis and clinical symptoms (*13*). The key finding for the diagnosis of Takayasu arteritis is the image analysis of angiograms, enhanced CT, and MRI showing the stenosis, occlusion, or aneurysm formation in large- and medium-sized vessels. The diagnosis of Takayasu arteritis often takes time because the discernable appearance of vascular lesions often takes time. We may hesitate to diagnose Takayasu arteritis in its early stage in suspected cases that do not have any vascular deformity. Therefore, direct identification of the inflammation in the vasculature facilitates the diagnosis of Takayasu arteritis in the early stage.

Several reports show the value of ^{18}F-FDG PET in the diagnosis of large vessel arteritis (*6–12*) and show strong ^{18}F-FDG signals in the vascular lesions that could be detected in several patients with aortitis. However, we found that ^{18}F-FDG PET analyses did not always give the strong signals that could be easily identified with a location anatomically in patients with active Takayasu arteritis. Coregistration of ^{18}F-FDG PET images with enhanced CT images has been described as a tool that provides good anatomic localization of functional data (*16,17*). Visual side-by-side analysis of nuclear medicine and CT studies is of value in characterizing large, single lesions (*18,19*). Therefore, we coregistered ^{18}F-FDG PET images with enhanced CT images to identify ^{18}F-FDG accumulation located in the vascular wall, to diagnose Takayasu arteritis, and also to exclude the cases of suspected Takayasu arteritis in which ^{18}F-FDG accumulation was not located on the vascular wall. Takayasu arteritis sometimes involves only pulmonary arteries (*20,21*), and it is difficult to diagnose because of few clinical symptoms. Our study shows that the coregistration of ^{18}F-FDG PET and enhanced CT may facilitate the diagnosis of isolated pulmonary arteritis due to Takayasu arteritis.

During the treatment of Takayasu arteritis with medication, general inflammatory markers such as C-reactive protein and erythrocyte sedimentation rate are used for the estimation of inflammatory activities. However, these inflammatory markers are reported to be unreliable surrogate markers for estimating the inflammatory activity of Takayasu arteritis during treatment with medication (*1*). Our study showed that C-reactive protein and erythrocyte sedimentation rate did not correlate with the existence of the inflammation in the vasculature. These findings suggest that ^{18}F-FDG PET may be a potential tool for estimating the disease activity of Takayasu arteritis. However, more cases must be studied to confirm these findings.

Pathologic analyses of Takayasu arteritis showed that the inflammatory process of Takayasu arteritis starts at the vasa vasorum in the adventitia (*2,22,23*). These inflammatory cells in the affected lesion may be involved in ^{18}F-FDG accumulation in Takayasu arteritis. Recently, ^{18}F-FDG PET was also used for the diagnosis of atherosclerosis (*24–26*). ^{18}F-FDG is believed to accumulate in atherosclerotic vascular lesions. Takayasu arteritis generally affects young females (*27*). They usually have a low number of risk factors for atherosclerosis and marked atherosclerosis formation is usually not expected in these young females. To differentiate ^{18}F-FDG accumulation due to Takayasu arteritis from atherosclerosis, the disappearance of ^{18}F-FDG accumulations during the treatment with medication may be a critical point. ^{18}F-FDG accumulation in PET in the diagnosis of Takayasu arteritis should be carefully interpreted along with other clinical findings.

CONCLUSION

Coregistration of ^{18}F-FDG PET and enhanced CT showed the distribution of the inflammation in the aorta, its branches, and the pulmonary artery. ^{18}F-FDG PET also reveals the disease activity of Takayasu arteritis directly and the general inflammatory markers did not necessarily coincide with disease activity shown by ^{18}F-FDG PET during the treatment with medication. These findings suggest that ^{18}F-FDG accumulation observed in Takayasu arteritis directly indicates the inflammation in the vascular wall. ^{18}F-FDG PET coregistered with enhanced CT should be useful in the diagnosis and management of Takayasu arteritis.

ACKNOWLEDGMENTS

We thank Professor Shoichi Ozaki of the University of St. Marianna, Kawasaki, Japan; Dr. Shigeto Kobayashi of Juntendo University, Tokyo, Japan; and Dr. Takamichi Miyamoto of Musashino Red Cross Hospital, Tokyo, Japan, for the enrollment of their patients to this study. We also

thank Professor Brian Mandell of The Cleveland Clinic, Cleveland, Ohio, for critical reading of the manuscript and discussion. This study was supported in part by a Grant-in-aid from the Ministry of Health, Labor, and Welfare, Japanese Government.

REFERENCES

1. Kerr GS, Hallahan CW, Giordano J, et al. Takayasu arteritis. *Ann Intern Med.* 1994;120:919–929.
2. Numano F. Vasa vasoritis, vasculitis and atherosclerosis. *Int J Cardiol.* 2000; 75(suppl 1):S1–S8.
3. Hoffman GS, Ahmed AE. Surrogate markers of disease activity in patients with Takayasu arteritis: a preliminary report from the International Network for the Study of the Systemic Vasculitides (INSSYS). *Int J Cardiol.* 1998;66(suppl)1: S191–S194.
4. Flamm SD, White RD, Hoffman GS. The clinical application of 'edema-weighted' magnetic resonance imaging in the assessment of Takayasu's arteritis. *Int J Cardiol.* 1998;66(suppl 1):S151–S159.
5. Tso E, Flamm SD, White RD, Schvartzman PR, Mascha E, Hoffman GS. Takayasu arteritis: utility and limitations of magnetic resonance imaging in diagnosis and treatment. *Arthritis Rheum.* 2002;46:1634–1642.
6. Hara M, Goodman PC, Leder RA. FDG-PET finding in early-phase Takayasu arteritis. *J Comput Assist Tomogr.* 1999;23:16–18.
7. Belhocine T, Blockmans D, Hustinx R, Vandevivere J, Mortelmans L. Imaging of large vessel vasculitis with ^{18}FDG PET: illusion or reality?—A critical review of the literature data. *Eur J Nucl Med Mol Imaging.* 2003;30:1305–1313.
8. Wenger M, Gasser R, Donnemiller E, et al. Images in cardiovascular medicine: generalized large vessel arteritis visualized by ^{18}fluorodeoxyglucose-positron emission tomography [letter]. *Circulation.* 2003;107:923.
9. Webb M, Chambers A, AL-Nahhas A, et al. The role of ^{18}F-FDG PET in characterising disease activity in Takayasu arteritis. *Eur J Nucl Med Mol Imaging.* 2004;31:627–634.
10. Meller J, Strutz F, Siefker U, et al. Early diagnosis and follow-up of aortitis with [^{18}F]FDG PET and MRI. *Eur J Nucl Med Mol Imaging.* 2003;30:730–736.
11. Meller J, Grabbe E, Becker W, Vosshenrich R. Value of F-18 FDG hybrid camera PET and MRI in early Takayasu aortitis. *Eur Radiol.* 2003;13:400–405.
12. Kissin EY, Merkel PA. Diagnostic imaging in Takayasu arteritis. *Curr Opin Rheumatol.* 2004;16:31–37.
13. Arend WP, Michel BA, Bloch DA, et al. The American College of Rheumatology 1990 Criteria for the Classification of Takayasu Arteritis. *Arthritis Rheum.* 1990;33:1129–1134.
14. Meikle SR, Bailey DL, Hooper PK, et al. Simultaneous emission and transmission measurements for attenuation correction in whole-body PET. *J Nucl Med.* 1995;36:1680–1688.
15. Kitamura K, Iida H, Shidahara M, Miura S, Kanno I. Noise reduction in PET attenuation correction using non-linear gaussian filters. *IEEE Trans Nucl Sci.* 2000;47:994–999.
16. Weber DA, Ivanovic M. Correlative image registration. *Semin Nucl Med.* 1994; 24:311–323.
17. Wahl RL, Quint LE, Cieslak RD, Aisen AM, Koeppe RA, Meyer CR. "Anatometabolic" tumor imaging: fusion of FDG PET with CT or MRI to localize foci of increased activity. *J Nucl Med.* 1993;34:1190–1197.
18. Correia JA. Registration of nuclear medicine images. *J Nucl Med.* 1990;31:1227–1229.
19. Shreve PD. Adding structure to function. *J Nucl Med.* 2000;41:1380–1382.
20. Lie JT. Pathology of isolated nonclassical and catastrophic manifestations of Takayasu arteritis. *Int J Cardiol.* 1998;66(suppl 1):S11–S21.
21. Lie JT. Isolated pulmonary Takayasu arteritis: clinicopathologic characteristics. *Mod Pathol.* 1996;9:469–474.
22. Noguchi S, Numano F, Gravanis MB, Wilcox JN. Increased levels of soluble forms of adhesion molecules in Takayasu arteritis. *Int J Cardiol.* 1998; 66(suppl)1:S23–S33.
23. Hotchi M. Pathological studies on Takayasu arteritis. *Heart Vessels.* 1992; 7(suppl):S11–S17.
24. Rudd JH, Warburton EA, Fryer TD, et al. Imaging atherosclerotic plaque inflammation with [^{18}F]-fluorodeoxyglucose positron emission tomography. *Circulation.* 2002;105:2708–2711.
25. Yun M, Yeh D, Araujo LI, Jang S, Newberg A, Alavi A. F-18 FDG uptake in the large arteries: a new observation. *Clin Nucl Med.* 2001;26:314–319.
26. Yun M, Jang S, Cucchiara A, Newberg AB, Alavi A. ^{18}F FDG uptake in the large arteries: a correlation study with the atherogenic risk factors. *Semin Nucl Med.* 2002;32:70–76.
27. Numano F, Okawara M, Inomata H, Kobayashi Y. Takayasu's arteritis. *Lancet.* 2000;356:1023–1025.

ORIGINAL ARTICLE

Annals of Nuclear Medicine Vol. 19, No. 6, 425–433, 2005

Use of reference tissue models for quantification of histamine H_1 receptors in human brain by using positron emission tomography and [^{11}C]doxepin

Atsuro SUZUKI,* Manabu TASHIRO,** Yuichi KIMURA,*** Hideki MOCHIZUKI,**** Kenji ISHII,*** Hiroshi WATABE,***** Kazuhiko YANAI,**** Kiichi ISHIWATA*** and Keizo ISHII*

*Department of Quantum Science and Energy Engineering, Tohoku University
**Cyclotron and Radioisotope Center, Tohoku University
***Positron Medical Center, Tokyo Metropolitan Institute of Gerontology
****Department of Pharmacology, Tohoku University School of Medicine
*****Department of Investigative Radiology, Research Institute, National Cardiovascular Center

The aim of the present study is to evaluate the validity of the simplified reference tissue model (SRTM) and of Logan graphical analysis with reference tissue (LGAR) for quantification of histamine H_1 receptors (H1Rs) by using positron emission tomography (PET) with [^{11}C]doxepin. These model-based analytic methods (SRTM and LGAR) are compared to Logan graphical analysis (LGA) and to the one-tissue model (1TM), using complete datasets obtained from 5 healthy volunteers. Since H1R concentration in the cerebellum can be regarded as negligibly small, the cerebellum was selected as the reference tissue in the present study. The comparison of binding potential (*BP*) values estimated by LGAR and 1TM showed good agreement; on the other hand, SRTM turned out to be unstable concerning parameter estimation in several regions of the brain. By including the results of noise analysis, LGAR became a reliable method for parameter estimation of [^{11}C]doxepin data in the cortical regions.

Key words: model-based analysis, histamine H_1 receptor, [^{11}C]doxepin, PET

INTRODUCTION

THE HISTAMINERGIC NEURON SYSTEM in the brain plays important roles in various physiological functions such as wakefulness, cognition and memory.[1–3] These brain functions are mediated mainly by histamine H_1 receptors (H1Rs), one of 4 known subtypes (H_1, H_2, H_3, and H_4).[1] For mapping the distribution of H1Rs in the human brain, positron emission tomography (PET) has been used with [^{11}C]-labeled doxepin, a potent H1R antagonist.[4] [^{11}C]doxepin is radiotracer of choice because of its high affinity to H1Rs and its ability to penetrate the blood-brain barrier.[5] PET with [^{11}C]doxepin has been applied to the investigation of various pathological states including Alzheimer's disease and epilepsy,[6,7] as well as sedation due to antihistamines observed in patients with various disorders.[2,8–10]

In most H1R mapping studies, the binding potential (*BP*) of [^{11}C]doxepin to H1Rs is calculated using the graphical method introduced by Logan and colleagues.[11] As part of our recent efforts to establish a suitable analytical method for [^{11}C]doxepin, we first demonstrated that the one-tissue model (1TM) was more stable in parameter estimation of [^{11}C]doxepin kinetics than the two-tissue model (2TM) which leads to a large variation in parameter values, depending strongly upon the startup parameters.[12] Thereafter, we also developed a short (15-min-long) static scan protocol of one-point blood sampling to reduce physical and psychological stress of test persons in clinical trials, in which the persons are to be scanned 3 to 4 times.[13] So far, we have not examined the possible application of reference tissue models to [^{11}C]doxepin data, where blood sampling is not needed. Two major reference tissue models are available: the simplified reference tissue model (SRTM)[14] and Logan graphical analysis with

Received November 15, 2004, revision accepted March 16, 2005.

For reprint contact: Keizo Ishii, D.Sci., Department of Quantum Science and Energy Engineering, Tohoku University, Aramaki-aza-aoba 01, Aoba-ku, Sendai 980–8579, JAPAN.
E-mail: keizo.ishii@qse.tohoku.ac.jp

reference tissue (LGAR).[15]

A compartment model for receptor analysis should be developed based on the kinetic tracer behavior in target organs. Usually, this behavior is described with a three-compartment model (two-tissue model: 2TM),[16] but if rapid equilibrium occurs among free, nonspecifically and specifically bound compartments, a 1TM is suitable for the kinetic analysis.[17] In fact, our previous study already demonstrated that 1TM was suitable for describing the kinetic data of [^{11}C]doxepin whereas the results based on 2TM highly depended on initial parameter estimation so that different initial values produced different results.[12] Therefore, 2TM was excluded from the present evaluation. In the present study, H1R-[^{11}C]doxepin binding parameters estimated by 2 reference tissue models, SRTM and LGAR, were compared to those calculated by LGA and by 1TM. Reliability of these analytical methods was also examined by comparing the obtained parameters to those calculated by 1TM, probably the most reliable method in the present evaluation.

MATERIALS AND METHODS

Subjects

Five healthy male volunteers, 21–27 years old, participated in the present study. None had any previous history of psychiatric or neurological disorders and none of them showed anatomical abnormalities in brain MRI images. Written informed consent was obtained from every subject before enrollment in the present study. The volunteers were asked to abstain from taking medication for a week before the study, and from taking tobacco, alcohol and caffeine on the day of experiment. The study was approved by the respective ethics committees of the Tokyo Metropolitan Institute of Gerontology and of Tohoku University Graduate School of Medicine, and was performed in compliance with relevant laws.

PET measurement

Dynamic scans in two-dimensional mode were performed using Headtome-V (Shimadzu Co., Kyoto, Japan) with 63 slices of 128-by-128 voxels each at transverse resolution of 4.5 mm full width of half maximum (FWHM) and at axial resolution of 5.8 mm FWHM. PET images were reconstructed with a filtered backprojection algorithm, and corrections were applied for dead time, detector uniformity and photon attenuation. The frame arrangement was 10 sec × 6 frames, 30 sec × 3 frames, 60 sec × 5 frames, 2.5 min × 5 frames and 5 min × 14 frames for a total of 90 minutes and [^{11}C]doxepin was prepared as previously described.[12] The injected radioactivity dose of [^{11}C]doxepin was 493 ± 109 MBq and the cold mass was 23 ± 16 nmol (mean ± SD). Arterial blood was sampled every 10 sec for the first 150 sec post-injection and afterwards at 3, 5, 7, 10, 15, 20, 30, 40, 50, 60, 75 and 90 min. Metabolite analysis was carried out using 6 plasma samples obtained 3, 10, 20, 30, 40 and 60 min after the injection as previously described.[12]

Model-based analysis

The 2TM provides a general framework for model-based analysis that consists of a plasma compartment (C_p) and two-tissue compartments: one compartment is for the free and nonspecifically bound ligands (C_{f+ns}), and the other is for the specifically bound ligands (C_s). The transfer of the ligand across compartments is governed by 4 fractional rate constants, K_1, k_2, k_3 and k_4, where K_1 is the influx rate constant into C_{f+ns}, k_2 is the efflux rate constant from C_{f+ns}, k_3 is the association rate constant into C_s, and k_4 is the dissociation rate constant from C_s, respectively. If the association and dissociation rates between free ligands and receptors are sufficiently rapid compared to the transport parameters K_1 and k_2, the model can be simplified using a one-tissue compartment, where all of the free ligands and nonspecifically and specifically bound ligands are represented by a single tissue compartment. This model is the 1TM,[17] where the concentration time function $C_T(t)$ in a certain regional tissue is expressed as follows,

$$C_T(t) = K_1 C_P(t) \otimes e^{-k_{2a}t} \quad (1)$$

where $C_P(t)$ is the concentration time function in the plasma, and k_{2a} is the efflux rate constant from the single tissue compartment. The distribution volume (DV) can be written as $DV = K_1/k_{2a} = K_1/k_2\,(1 + k_3/k_4)$. Provided that the H1R concentration in the reference tissue is negligibly small and that K_1/k_2 is constant in the all brain regions, the binding potential ($BP = k_3/k_4$) can be obtained as $BP = DV/DV^{REF} - 1$, where DV^{REF} is DV in the reference tissue. In the present study, the cerebellum was used as the reference tissue because of the negligibly small H1R concentration in this region.

In SRTM,[14] the target and reference tissues are described as a one-tissue model. If K_1/k_2 is constant in the all brain regions, $C_T(t)$ in the tissue is expressed as follows,

$$C_T(t) = R_1 C_R(t) + \left\{ k_2 - \frac{R_1 k_2}{1 + k_3/k_4} \right\} C_R(t) \otimes e^{-k_2/(1+k_3/k_4)t} \quad (2)$$

where $C_R(t)$ is the concentration time function in the reference region, and R_1 is the ratio of delivery to the regional tissue compared to the reference region (ratio of influx). This method can avoid the complexity of arterial blood sampling.

The formula for LGA is expressed as follows:[11]

$$\frac{\int_0^T C_T(t)dt}{C_T(T)} = DV \frac{\int_0^T C_P(t)dt}{C_T(T)} + a_1 \quad (3)$$

where the values of the slope DV and the intercept a_1 are obtained by linear regression. The BP value is obtained as $BP = DV/DV^{REF} - 1$. LGAR[15] is expressed as follows:

$$\frac{\int_0^T C_T(t)dt}{C_T(T)} = DVR\left(\frac{\int_0^T C_R(t)dt + C_R(t)/k_2'}{C_T(T)}\right) + a_2 \quad (4)$$

where DVR is the distribution volume ratio (DV/DV^{REF}), a_2 is an intercept term, and k_2' is an average value in the reference tissue. Then BP is obtained as $BP = DVR - 1$, and the complexity of arterial blood sampling is avoided.

Data analysis

Regions of interest (ROIs) were drawn on 5 cortical structures (the frontal, temporal, occipital, parietal and cingulate cortices) bilaterally, 3 subcortical structures (the thalamus, caudate nucleus and putamen) bilaterally, and on the midbrain centrally. Two ROIs in right and left regions were drawn on cortical and subcortical structures. In results, 17 ROI data were obtained to obtain averaged tissue time-activity curves (tTACs) as reported previously.[12] One additional ROI was drawn on the cerebellum to obtain an averaged tTAC in the reference tissue.

In 1TM and SRTM analysis, parameters were estimated in standard nonlinear fitting algorithms of the Gauss-Newton type. The nonlinear regression was considered to have converged if all parameters had been changed by less than 0.1% from the previous iteration. Failure of convergence was declared if nonlinear regression failed to reach convergence after 100 iterations, and if the determinant of the normal equation's coefficient matrix was less than 10^{-20}. The initial values of K_1 and k_2 in 1TM were 0.5 [ml/g/min] and 0.02 [/min], respectively, and those of R_1, k_2 and BP in SRTM were 1, 0.01 [/min] and 0.5, respectively. Delay between tTAC and the plasma time-activity curve (pTAC) was estimated using an averaged tTAC of the whole-brain. In the present study, cerebral blood volume was disregarded because it is generally small (3–5%).[18]

BP values derived from different methods were compared in terms of the following criteria: 1) failure rate, 2) physiological rationality, and 3) sensitivity to noise.

1) Failure rate

In general, a failure in parameter estimation occurs in the following cases: a) when the nonlinear regression procedure fails to reach convergence, b) when the estimated parameter is unstable against variation of the initial parameter values in nonlinear regression, c) when BP values calculated by $DVR - 1$ become negative, d) when the standard error in the estimated parameter becomes very large. Note that the standard error here means the error in a parameter caused by the inherent uncertainty of this estimation procedure. The standard error of the parameter was obtained from the diagonal of the covariance matrix, and the result of parameter estimation was defined as "failure" when the standard error exceeded 30%.[19] In the present analysis, a total of 85 ROIs (17 ROIs from each of 5 subjects) were examined. Then, the failure rate of each modeling procedure was expressed as [number of regions whose estimation failed]/85 × 100%.

2) Physiological rationality

Physiological rationality was assessed by comparing the estimated BP values to H1R densities measured in the brain *in vitro* using [^{3}H]doxepin, as reported by Kanba and Richelson.[20] In addition, correlations were examined between BP values calculated by 1TM and those by the other methods using Pearson's correlation test.

3) Sensitivity to noise

Simulation was performed to evaluate the sensitivity to noise for each model-based method. This evaluation was carried out for BP estimation for the temporal cortex that was rich in H1Rs and in the occipital cortex that was relatively poor in H1Rs, by using the cerebellum as the reference region. Simulation data (ROI_N) are expressed as the following:

$$ROI_N(t) = ROI(t) + SD(t) \times N(0,1) \quad (5)$$

$$SD(t) = \sqrt{\frac{c \times ROI(t) \times e^{\lambda t}}{\Delta t}}$$

where a non-dimensional constant c determines the noise level, λ is a decay constant of the isotope, Δt is frame length, $N(0,1)$ is a pseudo-random number of a Gauss distribution with zero mean and standard deviation of one.[21]

In the present simulation, random noise was introduced and noisy datasets were analyzed with SRTM, LGAR, LGA and 1TM, at 8 different noise levels (noise level c = 5, 10, 15, 20, 25, 30, 35, 40). The noise levels of the actual brain image data were considered to remain within the range of the noise levels mentioned above. In the present simulation analysis, 1000 different curves were generated for each noise level, and the effects of noise levels on the results were evaluated using a bias, i.e. the difference between the true BP values and BP values obtained in 1000 simulations, for each modeling method.

Simulation on the effect of nonspecific binding

In order to investigate the effect of nonspecific binding on the parameter estimation, another simulation was performed according to the following procedure. Simulated tTACs in the various cortical regions and the reference tissue (the cerebellum) were generated by 1TM with varying nonspecific binding values of DV^{REF} = 5, 10, 15, 20, 25, 30. Based on an assumption that nonspecific binding is equal in the target and reference regions, DV^{REF} was set to be identical to the nonspecific binding in the target regions in this simulation analysis. Based on the results of ROI analysis in the temporal cortex, the parameters K_1 and DV^{ROI} in the ROI were fixed at 0.495 [ml/g/min] and 36.5, respectively where DV^{ROI} represented the

Table 1 Calculated binding potential (*BP*) values using simplified reference tissue model (SRTM), Logan graphical analysis with reference tissue (LGAR), Logan graphical analysis (LGA) and one-tissue model (1TM), compared to histamine H_1 receptor (H1R) density in autopsied human brains.[20] In the frontal, temporal, occipital, parietal, and cingulate cortices, thalamus, caudate nucleus and putamen, mean ± SD of 10 ROIs (two ROIs in right and left regions for each of 5 subjects). In the midbrain, mean ± SD of 5 ROIs (one ROI for each of 5 subjects)

Brain areas	Estimated binding potential								H1R density measured *in vitro* (fmol/mg protein/0.1 nM)
	SRTM		LGAR		LGA		1TM		
	mean	%SD	mean	%SD	mean	%SD	mean	%SD	
frontal cortex	0.53	26	0.36	18	0.38	24	0.37	25	19.1
temporal cortex	0.51	14	0.47	16	0.49	25	0.49	24	23.5
parietal cortex	0.2	29	0.36	20	0.37	26	0.37	25	16.6
occipital cortex	0.35	34	0.24	21	0.25	19	0.25	16	13.2
cingulate cortex	—	—	0.39	19	0.39	20	0.4	21	22.3
thalamus	0.24	19	0.31	17	0.31	16	0.34	16	4.3
caudate nucleus	0.32	16	0.23	44	0.24	48	0.28	44	5.3
putamen	0.32	14	0.34	29	0.34	29	0.36	27	4.4
midbrain	—	—	0.16	146	0.22	110	0.14	148	2.2

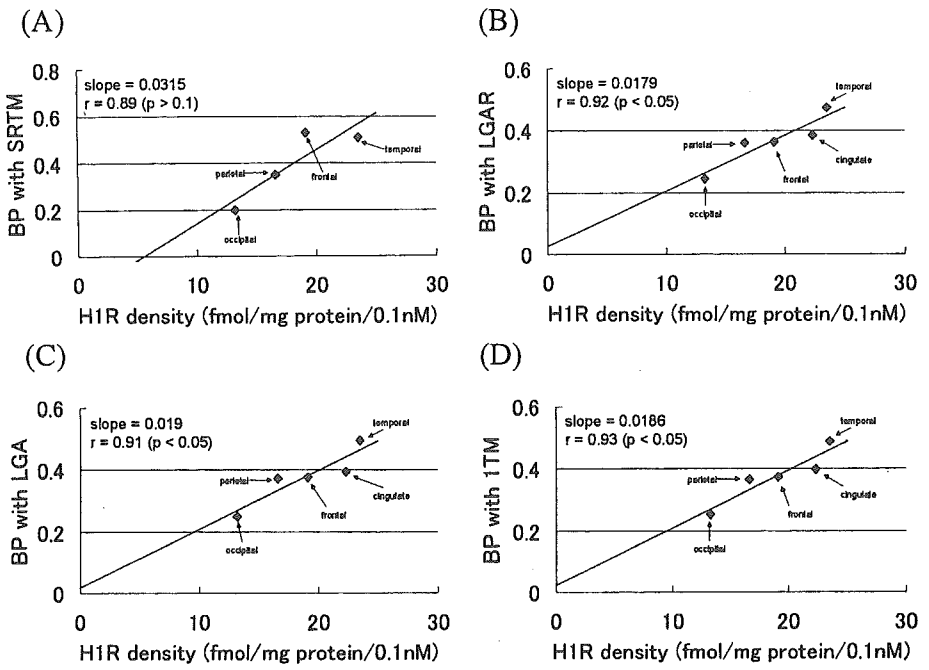

Fig. 1 Relationship between binding potential (*BP*) values and histamine H_1 receptor (H1R) densities in autopsied human brains.[20] The simplified reference tissue model (SRTM) (A), Logan graphical method with reference tissue (LGAR) (B), Logan graphical method with arterial sampling (LGA) (C), and one tissue model (1TM) (D).

sum of distribution volumes containing both nonspecific and specific bindings. The true *BP* values were calculated as $BP = DV^{ROI}/DV^{REF} - 1$. Since the DV^{ROI} value was fixed at 36.5 and DV^{REF} values were set to be changeable, high DV^{REF} values would result in low *BP* values. The parameter K_1 in the reference tissue was fixed at 0.529 [ml/g/min]. Random noise was introduced (noise level: c = 15) to the dynamic image data, and the noisy tTACs were analyzed with SRTM, LGAR, LGA and 1TM modeling methods at different DV^{REF} values, for which 1000 realizations of noisy tTACs were generated. Finally, the effect of nonspecific binding in the target and reference regions was evaluated by comparing *BP* estimates with the truth.

RESULTS

In the present study, *BP* values were calculated from *DV* or *DVR* values determined by each model using ROI-derived tTACs, and these *BP* values were then compared.

The mean cerebellar k_2 (0.022 [/min]) obtained by 1TM was used in LGAR. The averaged starting times t_0 for linear regression were 4.7 ± 1.7 [min] and 4.6 ± 1.8 [min] for LGA and LGAR, respectively.

Failure rate

Mean *BP* values estimated by SRTM, LGAR, LGA, and 1TM across the 5 subjects are presented in Table 1. In parameter estimation, 1TM produced reasonable *BP* values in all of 85 ROIs studied (failure rate = 0%), and LGA failed in 2 out of 85 ROIs (failure rate = 2.4%), respectively. SRTM, however, failed in 58 out of 85 ROIs (failure rate = 68.2%), while LGAR failed in only 1 out of 85 ROIs (failure rate = 1.2%).

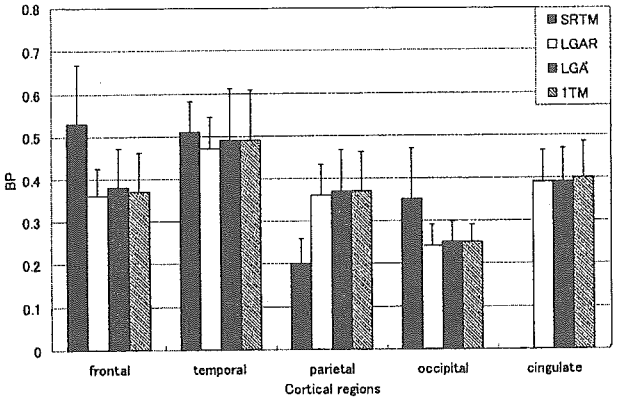

Fig. 2 Calculated binding potential (*BP*) values using simplified reference tissue model (SRTM), Logan graphical analysis with reference tissue (LGAR), Logan graphical analysis (LGA) and one-tissue model (1TM) in the five cortical regions (frontal, temporal, occipital, parietal and cingulate cortices). The *BP* value in the cingulate cortex was not available with SRTM.

Physiological rationality and correlation to results of 1TM

H1R densities in the human brain measured *in vitro* using [^{3}H]doxepin as a radioligand are given in Table 1.[20] H1R densities in the subcortical regions were lower than a quarter of the highest density in the cortex. However, a marked discrepancy in cortical/subcortical ratios was seen between the *BP* values measured *in vivo* and H1R densities measured *in vitro*. And the correlation between H1R densities and *BP* values was not statistically significant ($p > 0.05$) in the subcortical regions or in the midbrain for all of the 4 methods such as SRTM, LGAR, LGA and 1TM. Correlation of H1R densities to the *BP* values was statistically significant in the cortical regions such as the frontal, temporal, occipital, parietal and cingulate cortices, and the correlation coefficients were $r = 0.89$ ($p > 0.1$), $r = 0.92$ ($p < 0.05$), $r = 0.91$ ($p < 0.05$) and $r = 0.93$ ($p < 0.05$), respectively (Fig. 1).

In Figure 2, *BP* values in the 5 cortical regions are shown. Further correlation analysis demonstrated significant correlations of the BP values based on 1TM to those estimated by SRTM ($r = 0.73$: $p < 0.001$), LGAR ($r = 0.94$: $p < 0.001$) and by LGA ($r = 0.99$: $p < 0.001$), respectively

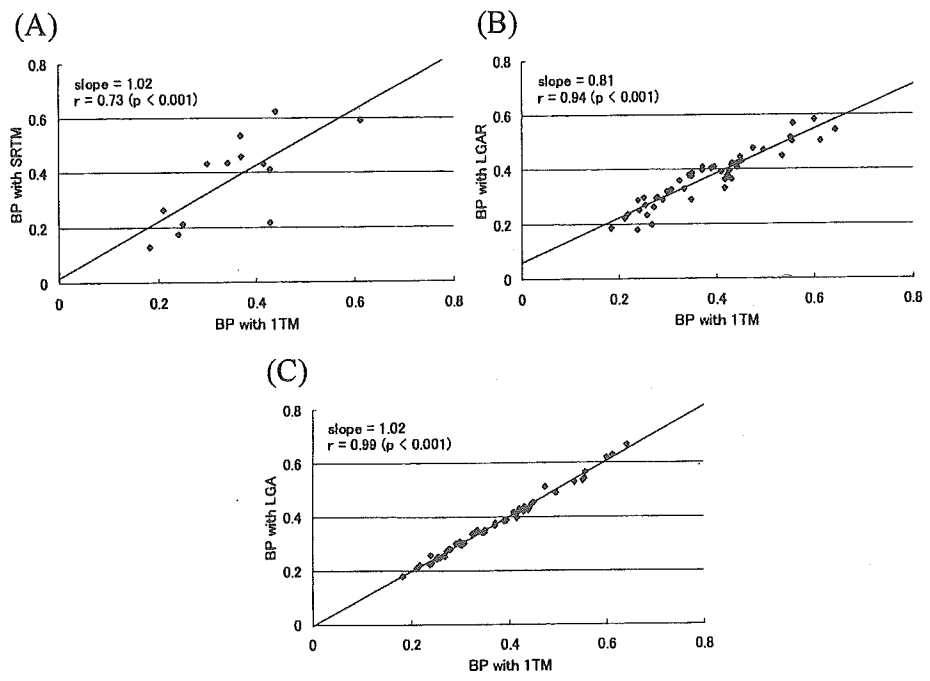

Fig. 3 Correlations between binding potential (*BP*) values calculated by 1TM and other three methods: the simplified reference tissue model (SRTM) (A), Logan graphical method with reference tissue (LGAR) (B), and Logan graphical method with arterial sampling (LGA) (C).

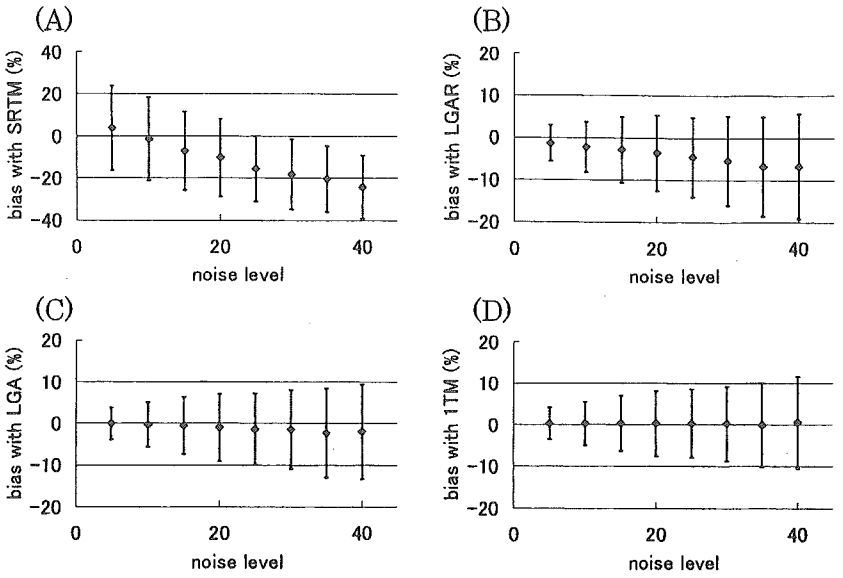

Fig. 4 Results of noise analysis in *BP* estimation in the temporal cortex with the simplified reference tissue model (SRTM) (A), Logan graphical method with reference tissue (LGAR) (B), Logan graphical method with arterial sampling (LGA) (C), and one tissue model (1TM) (D). The bias is between binding potential (*BP*) values averaged over 1000 simulations and the true *BP*. Noise level is described in MATERIALS AND METHODS section.

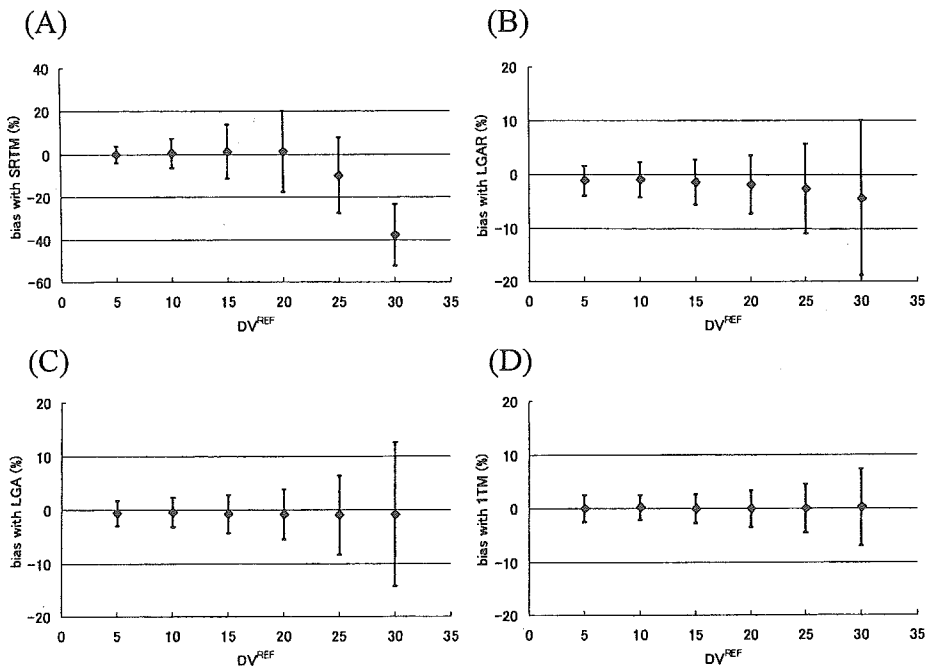

Fig. 5 Results of simulation in *BP* estimation at different DV^{REF}. The simplified reference tissue model (SRTM) (A), Logan graphical method with reference tissue (LGAR) (B), Logan graphical method with arterial sampling (LGA) (C), and one tissue model (1TM) (D). The bias is between binding potential (*BP*) values averaged over 1000 simulations and the true *BP*. Noise level *c* was fixed at 15.

(Fig. 3). The mean biases from the *BP* value based on 1TM (standard) in the cortical regions (50 ROIs: 10 ROIs for each of 5 subjects) were 6.5% with SRTM, 1.3% with LGAR and 0.3% with LGA, respectively.

Sensitivity to noise

The effect of noise in dynamic images on resultant *BP* values was examined for SRTM, LGAR, LGA and 1TM using simulation analysis. Simulated datasets were gener-

ated using TACs in the cerebellum (1TM, $K_1 = 0.529$ [ml/g/min], $k_2 = 0.0220$ [/min]), in the temporal cortex (1TM, $K_1 = 0.495$ [ml/g/min], $k_2 = 0.0140$ [/min]) and in the occipital cortex (1TM, $K_1 = 0.461$ [ml/g/min], $k_2 = 0.0153$ [/min]). Figure 4 shows results of the simulation for *BP* estimation in the temporal cortex. At all the noise levels studied here, the mean bias of *BP* values in 1TM was demonstrated to be smaller than in those of SRTM, LGAR and in LGA for both the temporal and the occipital cortices.

Simulation study on nonspecific binding

Figure 5 shows the results of simulation concerning *BP* estimation at different DV^{REF} values. As to the parameter estimation based on 1TM, biases were very small at all DV^{REF} values. In contrast, a trend toward an increased bias was observed with higher DV^{REF} values for LGA, LGAR and SRTM. Particularly, biases of SRTM at high DV^{REF} values were the largest among the all the methods examined. The results indicated that the failure rate of SRTM clearly increased with increased DV^{REF} values (for instance, 20, 25 and 30) ranging from 1.9, 28.0 to 66.5%, respectively, though the failure rate remained 0% when the DV^{REF} was smaller than 15. On the other hand, failure rates of 1TM, LGA and LGAR were always 0% at all given DV^{REF} values.

DISCUSSION

In the present study, the authors examined *BP* values estimated by SRTM and LGAR in terms of parameter stability and of correlation between autopsy data and *BP* values estimated by 1TM. An analytical method requiring arterial blood sampling is most accurate as the minimum bias and the highest correlation coefficients appear in the comparison of 1TM and LGA. However, it is difficult to apply this method to subjects in some situations such as in the presence of blood-borne infections.[15] Using reference tissue models, blood sampling and time-consuming metabolite measurements can be avoided and scanning protocol and data analysis can be simplified.[14]

Simplified reference tissue model (SRTM)

This method has been widely accepted and used for various tracers; however, this method was demonstrated to be unstable in parameter estimation of [^{11}C]doxepin binding. The failure rate of SRTM was so high (68.2%) that parameters were not available in many brain regions. The parameter correlation to 1TM was fairly low ($r = 0.71$: $p < 0.001$) and its correlation to autopsy data was not significant ($r = 0.89$: $p > 0.1$). The authors additionally tested the linear estimation method employed in Gunn's implementation of SRTM.[22] This method also failed to obtain *BP* values in 16 out of 85 ROIs (failure rate = 18.8%) even when the criterion 4 (standard error of the estimated parameter larger than 30%) was not applied. A possible reason for the high failure rate in parameter estimation with SRTM might be due to the relatively high nonspecific binding that resulted in a relatively large *DV* value in the cerebellum, which exceeded a half of the cortical *DV* values[5,12] (Table 2). Since *DV* values represent total binding, the cerebellar *DV* includes nonspecific binding while the cortical *DV* includes both specific and nonspecific bindings. Even if the amount of nonspecific binding is equal in the cortex and the cerebellum as described previously,[12] relatively high nonspecific binding might obscure the signals of specific binding in the cortex. According to Jensen and colleagues, SRTM seemed to be unsuitable for kinetic analysis for the binding of a serotonin transporter antagonist, [^{11}C]-NS 4194, because of its high nonspecific binding throughout the brain.[23]

Table 2 Calculated distribution volume (*DV*) values using Logan graphical analysis (LGA) and one-tissue model (1TM)

Brain areas	Present study *DV*			
	LGA		1TM	
	mean	%SD	mean	%SD
frontal cortex	33.6	19.4	33.6	19.7
temporal cortex	36.5	20.5	36.4	20.0
parietal cortex	33.5	18.9	33.4	19.2
occipital cortex	30.4	15.9	30.5	15.9
cingulate cortex	33.9	16.7	34.1	17.1
thalamus	32.0	16.1	32.5	15.3
caudate nucleus	30.3	20.6	31.4	21.3
putamen	32.7	19.4	33.2	19.3
midbrain	27.1	15.2	27.4	15.3
cerebellum	24.3	15.6	24.3	15.6

Thus, an additional simulation analysis was conducted in the present study in order to investigate the effect of nonspecific binding on the results of parameter estimation. The simulation analysis demonstrated that high nonspecific binding was associated with a high failure rate due to a large error in parameter estimation with SRTM, even when all required assumptions were fulfilled for the use of this model. The high failure rate due to high nonspecific binding can be predicted by the equation (2), where the high nonspecific binding reflects low k_2 values. Suppose the k_2 value is extremely low, the first term in the right-hand side is dominant and the right-hand side is almost independent of the second term which contains *BP*, k_2 and R_1. This would be one of the reasons parameters cannot be estimated uniquely. The mean k_2 value measured for [^{11}C]doxepin in the cerebellum was low (k_2 = 0.022 [/min]) as compared with that of other neuroreceptor radioligands such as the D_2-receptor antagonist [^{11}C]raclopride (0.163 [/min]) and the D_1-receptor antagonist [^{11}C]SCH23390 (0.101 [/min]).[24] Generally, SRTM appears to be suitable for tracers with negligibly low nonspecific binding in the reference tissues such as [^{11}C]raclopride and [^{11}C]SCH23390, but is not suitable for tracers with relatively high nonspecific binding

throughout the brain such as [^{11}C]doxepin.[14]

Logan graphical analysis with reference tissue (LGAR) This method[15] was introduced as an extended version of LGA[11] where tracer binding was evaluated as *DVR*. However, in order to calculate *BP* values expressed by *DVR* − 1, the two following assumptions are required.

The first assumption is that the region used as the reference is devoid of specific binding. Blocking studies showed that there is no appreciable difference in [^{11}C]doxepin binding in the cerebellum with or without administration of *d*-chlorpheniramine, a highly potent H1R antagonist[4,5] demonstrating that specific binding of [^{11}C]doxepin in the cerebellum is negligibly small. In addition, postmortem human studies revealed that the H1R density in the cerebellum was less than a tenth of that in the frontal cortex.[20,25] Thus, it appears that the first assumption is justified in the present case.

The second assumption states that K_1/k_2 should be equal in the target and reference tissues. It is impossible to directly prove that K_1/k_2 is equal in all the brain regions in the case of [^{11}C]doxepin since K_1, k_2, k_3 and k_4 were not available with 2TM.[12] However, a previous study demonstrated a similar amount of nonspecific binding in the cerebellum and cerebral cortices.[25] Thus the second assumption holds for the cortical tissues, and it appears to justify calculation of *BP* values with LGAR.

Furthermore, the excellent correlation between *BP* values estimated by LGAR and 1TM ($r = 0.96$: $p < 0.001$) justifies the use of the cerebellar ROI value as a reference input. The failure rates, one of the criteria for validation of these modeling methods, were 1.2%, 2.4% and 0% for LGAR, LGA and 1TM, respectively. Because the graphical analysis requires no apriori choice of compartment configuration, the correlation to *DV* values calculated by LGA is a possible criterion for choosing a compartment configuration.

The noise simulation demonstrated that 1TM provided better parameter estimation than LGA in the presence of noise (Fig. 4). In addition, the failure rate of 1TM was 0% and the correlation between *BP* with 1TM and biopsy data in the cortical regions was strong ($r = 0.93$). As described previously, 1TM described [^{11}C]doxepin kinetics better than 2TM.[12] Therefore, we chose 1TM as the reference in the present study. Comparison between H1R densities and *BP* values from LGAR, LGA and 1TM showed much better correlations in the cortical regions than in other brain regions. One of the reasons to explain this might be relatively high nonspecific binding in these regions.[25] Therefore, the parameters in the regions with high nonspecific binding should be evaluated with caution. On the other hand, since specific binding in the cortex is relatively high, *BP* estimation in the cortex is more reliable.

In the simulations to evaluate stability to noise, the bias of *BP* values from LGAR is larger than those obtained from LGA and 1TM at all noise levels. To determine the noise level corresponding to the noise level in actual brain image data, we compared the mean sum of squares of residuals in simulation data at each noise level to the ones of the actual image datasets. For *BP* estimation in the temporal cortex with LGAR, this comparison revealed that the noise level of actual brain image data corresponds to a noise level of 10 to 15 (Fig. 4) resulting in average bias of −2.2% to −2.8%. On the other hand, for *BP* estimation in the occipital cortex with LGAR, the noise level of actual brain image data corresponded to noise levels of 10 to 15 resulting here in average bias of −3.1% to −3.7%. These results suggest that reliable parameter estimation with small bias is provided by LGAR as long as the noise level of actual brain data remains around 10 to 15 in the cortex, although LGAR underestimates the true values, when the noise level of actual brain data is higher, as mentioned already.[26]

In summary, in the present study, we analyzed [^{11}C]doxepin binding with SRTM, LGAR, LGA and 1TM. Comparison of *BP* values estimated by LGAR showed an excellent correlation with 1TM. On the other hand, SRTM did not provide satisfactory parameter estimation in several brain regions. At the noise level of actual brain data, LGAR was able to provide reliable parameter estimation in the cortex with small bias. Since LGAR does not require arterial blood sampling, this method is a useful tool for clinical studies for H1R quantification with PET and [^{11}C]doxepin. This method can be applied to investigation of brain H1R densities in various physiological and pharmacological conditions in healthy and diseased subjects in the near future, although the present study used only a limited number of normal subjects ($n = 5$). We expect a growing number of nuclear medicine techniques will be applied in related fields using convenient methods as discussed in this paper.

ACKNOWLEDGMENTS

This work was partly supported by Grants-in-Aid from the Ministry of Education, Culture, Sports, Science, and Technology, and from the Ministry of Health, Labor and Welfare, Japan. The authors thank the volunteers in the PET measurement, Keiichi Oda, Ph.D. and Ms. Miyoko Ando for their help in PET measurements and Toru Sasaki, Ph.D. and Kazunori Kawamura, Ph.D. for the preparation of [^{11}C]doxepin. The authors also thank Professor Masatoshi Itoh, at Tohoku University Cyclotron and Radioisotope Center, for his valuable comments and advice.

REFERENCES

1. Haas H, Panula P. The role of histamine and the tuberomamillary nucleus in the nervous system. *Nat Rev Neurosci* 2003; 4 (2): 121–130.
2. Yanai K, Okamura N, Tagawa M, Itoh M, Watanabe T. New findings in pharmacological effects induced by antihista-

mines: from PET studies to knock-out mice. *Clin Exp Allergy* 1999; 29 Suppl 3: 29–36; discussion 37–38.
3. Huang ZL, Qu WM, Li WD, Mochizuki T, Eguchi N, Watanabe T, et al. Arousal effect of orexin A depends on activation of the histaminergic system. *Proc Natl Acad Sci USA* 2001; 98 (17): 9965–9970.
4. Yanai K, Watanabe T, Yokoyama H, Meguro K, Hatazawa J, Itoh M, et al. Histamine H_1 receptors in human brain visualized *in vivo* by [^{11}C]doxepin and positron emission tomography. *Neurosci Lett* 1992; 137 (2): 145–148.
5. Ishiwata K, Kawamura K, Wang WF, Tsukada H, Harada N, Mochizuki H, et al. Evaluation of *in vivo* selective binding of [^{11}C]doxepin to histamine H_1 receptors in five animal species. *Nucl Med Biol* 2004; 31 (4): 493–502.
6. Higuchi M, Yanai K, Okamura N, Meguro K, Arai H, Itoh M, et al. Histamine H(1) receptors in patients with Alzheimer's disease assessed by positron emission tomography. *Neuroscience* 2000; 99 (4): 721–729.
7. Iinuma K, Yokoyama H, Otsuki T, Yanai K, Watanabe T, Ido T, et al. Histamine H_1 receptors in complex partial seizures. *Lancet* 1993; 341 (8839): 238.
8. Yanai K, Ryu JH, Watanabe T, Iwata R, Ido T, Sawai Y, et al. Histamine H_1 receptor occupancy in human brains after single oral doses of histamine H_1 antagonists measured by positron emission tomography. *Br J Pharmacol* 1995; 116 (1): 1649–1655.
9. Tagawa M, Kano M, Okamura N, Higuchi M, Matsuda M, Mizuki Y, et al. Neuroimaging of histamine H_1-receptor occupancy in human brain by positron emission tomography (PET): a comparative study of ebastine, a second-generation antihistamine, and (+)-chlorpheniramine, a classical antihistamine. *Br J Clin Pharmacol* 2001; 52 (5): 501–509.
10. Tashiro M, Sakurada Y, Iwabuchi K, Mochizuki H, Kato M, Aoki M, et al. Central Effects of Fexofenadine and Cetirizine: Measurement of Psychomotor Performance, Subjective Sleepiness, and Brain Histamine H_1-Receptor Occupancy Using ^{11}C-Doxepin Positron Emission Tomography. *J Clin Pharmacol* 2004; 44 (8): 890–900.
11. Logan J, Fowler JS, Volkow ND, Wolf AP, Dewey SL, Schlyer DJ, et al. Graphical analysis of reversible radioligand binding from time-activity measurements applied to [*N*-^{11}C-methyl]-(−)-cocaine PET studies in human subjects. *J Cereb Blood Flow Metab* 1990; 10 (5): 740–747.
12. Mochizuki H, Kimura Y, Ishii K, Oda K, Sasaki T, Tashiro M, et al. Quantitative measurement of histamine H(1) receptors in human brains by PET and [^{11}C]doxepin. *Nucl Med Biol* 2004; 31 (2): 165–171.
13. Mochizuki H, Kimura Y, Ishii K, Oda K, Sasaki T, Tashiro M, et al. Simplified PET measurement for evaluating histamine H_1 receptors in human brains using [^{11}C]doxepin. *Nucl Med Biol* (in press).
14. Lammertsma AA, Hume SP. Simplified reference tissue model for PET receptor studies. *Neuroimage* 1996; 4 (3 Pt 1): 153–158.
15. Logan J, Fowler JS, Volkow ND, Wang GJ, Ding YS, Alexoff DL. Distribution volume ratios without blood sampling from graphical analysis of PET data. *J Cereb Blood Flow Metab* 1996; 16 (5): 834–840.
16. Mintun MA, Raichle ME, Kilbourn MR, Wooten GF, Welch MJ. A quantitative model for the *in vivo* assessment of drug binding sites with positron emission tomography. *Ann Neurol* 1984; 15 (3): 217–227.
17. Koeppe RA, Holthoff VA, Frey KA, Kilbourn MR, Kuhl DE. Compartmental analysis of [^{11}C]flumazenil kinetics for the estimation of ligand transport rate and receptor distribution using positron emission tomography. *J Cereb Blood Flow Metab* 1991; 11 (5): 735–744.
18. Phelps ME, Huang SC, Hoffman EJ, Kuhl DE. Validation of tomographic measurement of cerebral blood volume with C-11-labeled carboxyhemoglobin. *J Nucl Med* 1979; 20 (4): 328–334.
19. Carson RE, Parameters estimation in positron emission tomography. In: *Positron emission tomography. Principles and applications for the brain and the heart.* Phelps ME, Mazziotta JC, Schelbert HR (eds). New York; Raven Press, 1986: 347–390.
20. Kanba S, Richelson E. Histamine H_1 receptors in human brain labelled with [^{3}H]doxepin. *Brain Res* 1984; 304 (1): 1–7.
21. Kimura Y, Senda M, Alpert NM. Fast formation of statistically reliable FDG parametric images based on clustering and principal components. *Phys Med Biol* 2002; 47 (3): 455–468.
22. Gunn RN, Lammertsma AA, Hume SP, Cunningham VJ. Parametric imaging of ligand-receptor binding in PET using a simplified reference region model. *Neuroimage* 1997; 6 (4): 279–287.
23. Jensen SB, Smith DF, Bender D, Jakobsen S, Peters D, Nielsen EO. [^{11}C]-NS 4194 versus [^{11}C]-DASB for PET imaging of serotonin transporters in living porcine brain. *Synapse* 2003; 49: 170–177.
24. Sossi V, Holden JE, Chan G, Krzywinski M, Stoessl AJ, Ruth TJ. Analysis of four dopaminergic tracers kinetics using two different tissue input function methods. *J Cereb Blood Flow Metab* 2000; 20 (4): 653–660.
25. Yanai K, Watanabe T, Meguro K, Yokoyama H, Sato I, Sasano H, et al. Age-dependent decrease in histamine H_1 receptor in human brains revealed by PET. *Neuroreport* 1992; 3 (5): 433–436.
26. Logan J, Fowler JS, Ding YS, Franceschi D, Wang GJ, Volkow ND, et al. Strategy for the formation of parametric images under conditions of low injected radioactivity applied to PET studies with the irreversible monoamine oxidase A tracers [^{11}C]clorgyline and deuterium-substituted [^{11}C]clorgyline. *J Cereb Blood Flow Metab* 2002; 22 (11): 1367–1376.

Graefe's Arch Clin Exp Ophthalmol
(2005) 243: 576–582

CLINICAL INVESTIGATION

DOI 10.1007/s00417-004-1009-5

Shoichi Mizoguchi
Yukihisa Suzuki
Motohiro Kiyosawa
Manabu Mochizuki
Kenji Ishii

Differential activation of cerebral blood flow by stimulating amblyopic and fellow eye

Received: 7 May 2004
Accepted: 16 July 2004
Published online: 14 January 2005

S. Mizoguchi · Y. Suzuki ·
M. Kiyosawa (✉) · M. Mochizuki
Department of Ophthalmology and Visual Science, Tokyo Medical and Dental University Graduate School, Tokyo, Japan
e-mail: m.kiyosawa.oph@tmd.ac.jp
Tel.: +81-3-58035302
Fax: +81-3-38187188

S. Mizoguchi · Y. Suzuki ·
M. Kiyosawa · K. Ishii
Positron Medical Center, Tokyo Metropolitan Institute of Gerontology, Tokyo, Japan

Abstract *Purpose:* Positron emission tomography (PET), the blood flow response in the primary visual cortex (V1) to two visual stimuli, low temporal frequency (6 Hz) to activate the parvocellular system, and high temporal frequency (25 Hz) to activate the magnocellular system were used to investigate pathophysiologic mechanism of amblyopia. *Methods:* Five women and one man who were aged between 26 and 60 years, who were ophthalmologically normal except for amblyopia, and who had corrected visual acuity in the amblyopic eye of 0.6 or worse were examined. An intravenous injection of the $H_2{}^{15}O$ was given, and the regional cerebral blood flow was measured by PET during full-field stimulation with either 6 Hz or 25 Hz flicker to the amblyopic or the sound eye. *Result:* The activation of blood flow in the contra-lateral area V1 by the 6-Hz stimulation of the sound eye was greater than that during the stimulation of the amblyopic eye ($P<0.05$, small volume correction, $n=6$). With 25-Hz stimulation of the sound and amblyopic eyes, the blood flow in the contra-lateral and ipsi-lateral areas V1 was not significantly different. *Conclusion:* The decreased activation of blood flow in the contra-lateral V1 by low temporal frequency stimuli supports the hypothesis that the parvocellular pathway in amblyopic eyes is depressed.

Introduction

Amblyopia is an ocular disorder in which the visual acuity is depressed and uncorrectable with lenses in the absence of visible organic eye disease [2]. Although many hypotheses have been proposed for the mechanism of amblyopia, the general consensus is that amblyopia is caused by an abnormal development of the visual areas of the brain because of abnormal visual stimulation during early visual development [12]. Amblyopia is found in patients with strabismus, anisometropia, stimulus deprivation in eyes with congenital cataract, and other conditions that prevent the formation of a clear image on the retina. The frequency of amblyopia is 2% or 3% of the general population [5].

In cats and monkeys, Hubel and Wiesel first reported that form visual deprivation affected both the visual cortices and the lateral geniculate nuclei (LGN) [15, 16]. Von Noorden et al. reported that the cells in the parvocelluar layers of the LGN receiving input from contra-lateral fibers were predominantly shrunken compared with those receiving input from ipsi-lateral fibers in a patient with anisometropic amblyopia [27]. Studies with visual evoked potentials and functional magnetic resonance imaging (fMRI) have demonstrated that the responses to lower temporal frequencies [3] and higher spatial frequencies [3, 20, 25] are reduced in amblyopia.

Two functional pathways are present in the visual system: a parvocellular pathway that mainly carries visual information consisting of lower temporal frequencies and higher spatial frequencies, and a magnocelluar pathway that mainly carries information of higher temporal frequencies and lower spatial frequencies [24].

The purpose of this study was to determine whether the blood flow in the visual cortex was different when the

amblyopic eye was stimulated from that when the sound fellow eye was stimulated. In addition, the blood flow in the visual cortex was measured when the amblyopic or fellow eye was stimulated with low temporal frequency (6 Hz) to activate the parvocellular system or by high temporal frequency (25 Hz) stimuli to activate the magnocellular system. Positron emission tomography (PET) was used to measure the blood flow in the visual cortices.

Previous functional neuroimaging studies of amblyopia reported an altered response of the visual cortex when the amblyopic eye was stimulated [1, 3, 4, 6–8, 11, 17, 18, 20]; however, the responses in ipsi-lateral V1 and contra-lateral V1 to the side of the stimulation were not differentiated. Miki et al. [21, 22] reported in their fMRI study of normal subjects that the ipsi-lateral and the contra-lateral V1 were activated differently by monocular full-field visual stimuli. In view of the pathological evidence reported by von Noorden et al. [27], it is thus necessary to examine the function of ipsi-lateral and contra-lateral LGN separately. We therefore flipped all the PET images with left eye stimulation so that the stimulated eye could be placed on the right side, so that we could make a direct comparison between ipsi-lateral or contra-lateral sides of the sound and amblyopic eyes.

Materials and methods

Subjects

Six patients with unilateral amblyopia but with no ophthalmological or neurological abnormalities were studied. Their ages ranged from 26 to 60 years with a mean ± SD of 44.8±13.2 years (Table 1). All the patients had routine MRI scans of the brain before the PET study in order to rule out organic brain disorders. The study protocol was approved by the Institutional Ethics Committee of the Tokyo Metropolitan Institute of Gerontology, and a written informed consent was obtained from each subject.

PET measurements

Each subject was placed in a supine position in the PET camera gantry with their heads immobilized by a customized molded plastic head holder. Scans were acquired with a PET camera, viz., the Headtome-V SET 2400W scanner (Shimadzu, Kyoto, Japan), which provided 50 planes at an interval of 3.125 mm.

The visual stimuli were started 30 s before the intravenous injection of a bolus of 150 MBq [^{15}O] H_2O, and a 2-min emission scan was started at the time of the injection. The regional cerebral blood flow (rCBF) was calculated by the PET autoradiographic method [13].

The scanning room was dimly lit, and all the subjects wore goggles throughout the PET study. Electrooculography (EOG) was used to monitor eye movements and blinking during the PET measurements. Methods were otherwise as described in detail elsewhere [19, 23].

Visual tasks

Five visual tasks were used during the PET study. The first task was resting with both eyes closed (rest) while lying on the bed of the scanner in a supine position. The subjects were instructed to be relaxed and not move their eyelids or any other parts of their bodies. In brief, the second through fifth tasks consisted of full-field flicker stimulation by red-light-emitting diodes mounted in the goggles (5×3 LEDs; Signal Processor 7S12, NEC, Tokyo).

In more detail, the second task was 6-Hz flicker stimulation of the sound eye, and the third task was 25-Hz flicker stimulation to the sound eye. The fourth task was 6-Hz flicker stimulation to the amblyopic eye, and the fifth task was 25-Hz flicker stimulation to the amblyopic eye. The duration of the stimulus train was 80 ms at 6 Hz and 20 ms at 25 Hz so that the mean luminance was 280 cd/m^2 for both 6 Hz and 25 Hz. These five conditions were repeated twice in a random order to cancel out the effects of order of measurements.

Table 1 Ophthalmological findings of six unilateral ambyopic patients (*M* male, *F* female, *RE* right eye, *LE* left eye, *Aniso* anisometropic amblyopia, *Strab* strabismic amblyopia, *PD* prism diopter, *Ortho* orthotropia, *Eso* esotropia, *Exo* exotropia, *Ds* spherical lens diopter, *Dc* cylinder lens diopter)

Case/age (year)/sex	Amblyopic eye/type	Strabismic deviation (PD)	Refractive correction	
			Normal eyes	Amblyopic eyes
1/53/F	LE/Aniso	Ortho	1.0−1.00Ds = 0.75DcA90	0.6−2.00Ds = −5.00DcA90
2/60/F	LE/Aniso	Ortho	1.0−1.75Ds	0.1+3.00Ds = −0.50DcA95
3/26/F	LE/Aniso	Ortho	1.0+0.25Ds = −0.50DcA50	0.4+3.50Ds = −0.50DcA180
4/39/F	LE/Strab	Eso, 50	1.0−0.50DcA75	0.01+1.00Ds
5/36/F	RE/Strab	Eso, 40	1.0+1.25Ds = 0.75DcA90	0.1+0.50Ds
6/55/M	LE/Strab	Exo, 45	1.0+1.25Ds = 0.25DcA180	0.1+3.00Ds = −0.50DcA180